Molecular motors: new designs and applications

Roke, Gerrit Dirk

Chapter 3
Tunable visible light driven molecular motors based on oxindole

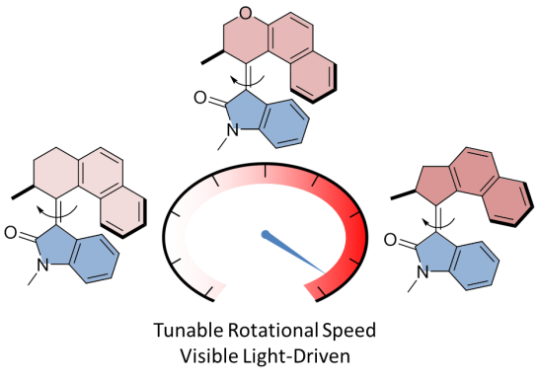

Molecular rotary motors based on oxindole which can be driven by visible light are presented. This novel class of motors can be easily synthesized in a Knoevenagel condensation and the choice of different upper halves allows for the facile tuning of their rotational speed. Their four-step rotational cycle was explored using DFT calculations and the expected photochemical and thermal isomerization behavior for molecular rotary motors was confirmed by NMR, UV/vis and CD spectroscopy. These oxindole motors are offer attractive prospects for functional molecular materials.

This chapter will be published as: D. Roke, M. Sen, W. Danowski, S. J. Wezenberg, B. L. Feringa, *Manuscript in preparation*

3.1 Introduction

The emergence of artificial molecular machines has allowed chemist to control movement at the molecular scale.[1–7] Among these machines, molecular rotary motors are drawing a lot of attention owing to their unique ability to undergo repetitive unidirectional rotational motion.[8–10] Overcrowded alkene-based motors, which are driven by light, have shown great potential in a number of fields, such as soft materials,[11–14] catalysis[15] and surface chemistry.[16] They were first reported by our group in 1999,[17] and since then, second and third generation molecular motors have been developed and their functioning has been thoroughly investigated.[18,19] Through synthetic modification, their rotational speed can be tuned,[8,20,21] and recently methods to control their speed dynamically have been developed.[22–24] A major challenge that remains is to drive the rotation with visible light instead of harmful UV light.[25] Strategies to shift the excitation wavelength to the visible range have been developed by, for example, making use of photosensitizers,[22,26] extended π systems,[27] or push-pull substituents.[28] However, for molecular motors to fully reach their potential, there are a number of challenges that still need to be addressed.[9,10] They should, for example, be powered with a sustainable energy source.

Apart from adapting the design of existing motors, new types of light driven molecular motors have appeared. Lehn and coworkers reported easily accessible molecular motors based on imines,.[29,30] and the group of Dube developed molecular motors based on hemithioindigo, which can be operated with visible light.[31,32] Here we present a design that is based on arylidene oxindoles, which are easily accessed by a condensation reaction and can be operated by visible light.

The group of Luňák Jr. has shown that some arylidene oxindoles undergo *E*-*Z* isomerization when exposed to sunlight, but the potential of these compounds as photoswitches was not explored.[33] Inspired by the facile synthesis and the interesting spectroscopic properties of arylidene oxindoles, we envisioned a new design for a molecular rotary motor (Scheme 3.1).

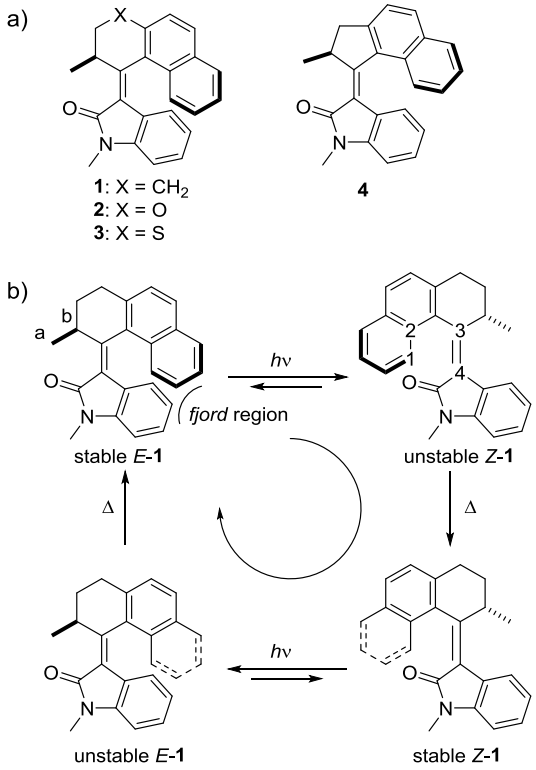

*Scheme 3.1. a) Oxindole-based molecular motors b) Representative rotational cycle of motor **1***

3.2 DFT calculations

Initially, DFT calculations were performed to predict the structural parameters and the relative energies of the different isomers of oxindole-based motors **1-4** (Figure 3.2). All structures were optimized using the B3LYP functional with a 6-31+G(d,p) basis set. Additionally, a IEFPCM, DMSO solvation model was chosen as previous studies with arylidene oxindoles were carried out in DMSO.[33] The calculated relative Gibbs free energies of all stable and unstable states, as well as the transition states (TS) for THI are shown in Figure 3.1. In all cases, two unstable states are found that are much higher in energy than their respective stable states with opposite helicity. This energy difference is crucial to assure unidirectionality in the rotary cycle of molecular motors. The relative energy barriers for THI of all motors are summarized in Table 3.1.

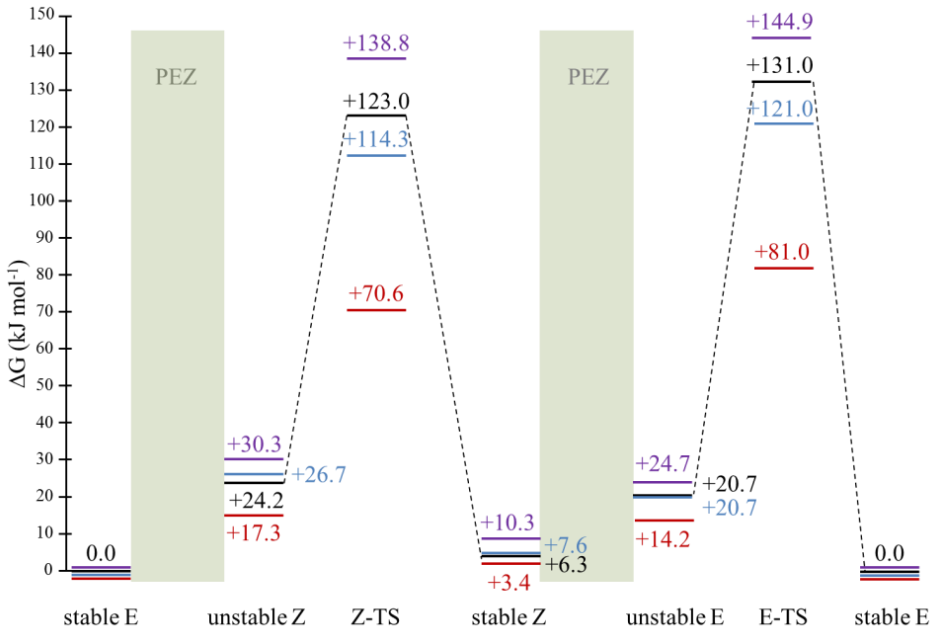

*Figure 3.1. Calculated relative Gibbs free energies of motors **1** (black), **2** (blue), **3** (purple) and **4** (red).*

Similar to what has been reported for their overcrowded alkene-based counterparts,[34,36] motors **1-3** with a central six membered ring in the upper half have higher barriers than motor **4** with a five membered ring. The latter has less steric hindrance in the *fjord* region, making it easier for the two halves to slip along each other. In all cases, the barrier for THI of unstable-*Z* is lower than for unstable-*E* which can also be explained by less steric hindrance in the *fjord* region as here the upper half needs to pass the smaller carbonyl instead of the bulkier aromatic ring. Furthermore, the calculated barriers for THI in motors **1-3** scale with the size of the bridging atom X (S > C > O). The upper half is pushed closer towards the lower half as the size of X increases, causing more steric hindrance in the *fjord* region. As a consequence, the upper half folds away from the lower half, resulting in an increased dihedral angle 1-2-3-4 in unstable-*Z* (Table 3.1). A similar effect has been observed in structurally related molecular motors.[35] The results of these calculations indicate that oxindole-based molecular motors **1-4** will operate as unidirectional rotary molecular motors.

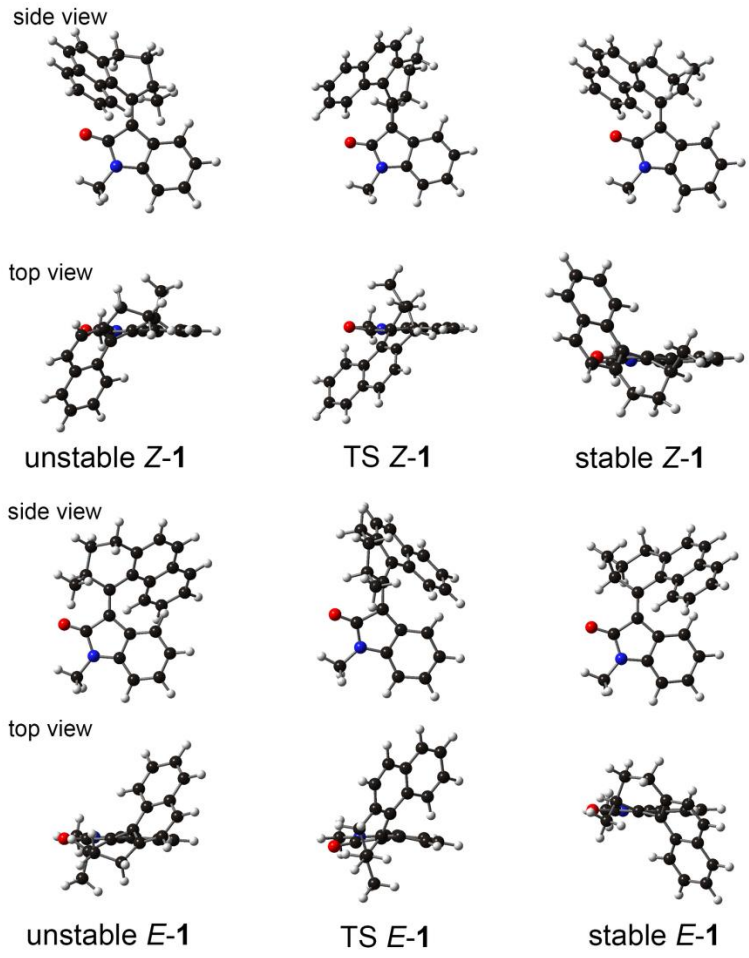

*Figure 3.2. DFT optimized structures of motor **1** as a representative example.*

	$\Delta^{\ddagger}G^{calc}$ (Z) (kJ mol^{-1})	$\Delta^{\ddagger}G^{calc}$ (E) (kJ mol^{-1})	Dihedral angle[a]
1	98.8	110.3	43.1
2	87.6	100.4	41.2
3	108.5	120.2	48.1
4	53.3	66.8	23.9

*Table 3.1. DFT calculated barriers for THI of **1**-**4**. [a] Dihedral angle 1-2-3-4 as shown in Scheme 3.1 of unstable Z.*

3.3 Synthesis

Oxindole motors **1-4** were synthesized in a single step by a Knoevenagel condension of commercially available *N*-methyloxindole and the corresponding ketone, mediated by a combination of $TiCl_4$ and DBU (Scheme 3.2). The ketones were synthesized in one to four steps following well-established literature procedures,[35,37] thus making these molecular motors very easily accessible. In all cases the *E*-isomer was exclusively obtained. According to DFT calculations, this isomer is the most stable one (*vide infra*). The structures of the molecular motors **1**-**4** were determined by ^{1}H and ^{13}C-NMR, and UV/vis spectroscopy and composition by HRMS.

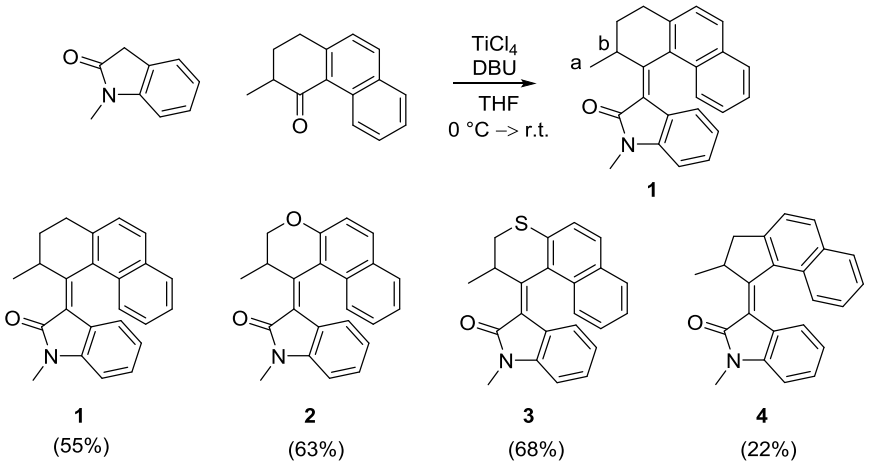

*Scheme 3.2. Representative synthesis of molecular motor **1** and isolated yields of **1-4**.*

3.4 ^{1}H-NMR studies

With these four different motors in hand, the photochemical and thermal isomerization behavior was first monitored by ^{1}H-NMR spectroscopy with 365 nm light. Upon irradiation of an NMR sample of *E*-**1** in DMSO-d_6 at room temperature, a new set of signals appeared (Figure 3.3). The most distinct shifts were observed for protons H_a (1.02 -> 1.39) and H_b (4.48 -> 4.02) at the stereogenic center (see Scheme 3.1 for the atom labeling). Hence, these ^{1}H-NMR spectral changes were ascribed to formation of the unstable *Z*-isomer. The sample was irradiated until no further changes were observed and at this photostationary state (PSS) the ratio of unstable *Z*-**1** to stable *E*-**1** was 76:24. Heating this sample to 60 °C resulted in the disappearance of the signals assigned to this photogenerated isomer. A new stable state was obtained and isolation and characterization of the newly obtained isomer on preparative scale revealed that this isomer is the stable *Z*-isomer. This confirms that the oxindole-based motor undergoes an *E*-*Z*-isomerization upon irradiation which, followed by a subsequent THI to complete 180° rotation, identical to other molecular motors based overcrowded alkenes.[17]

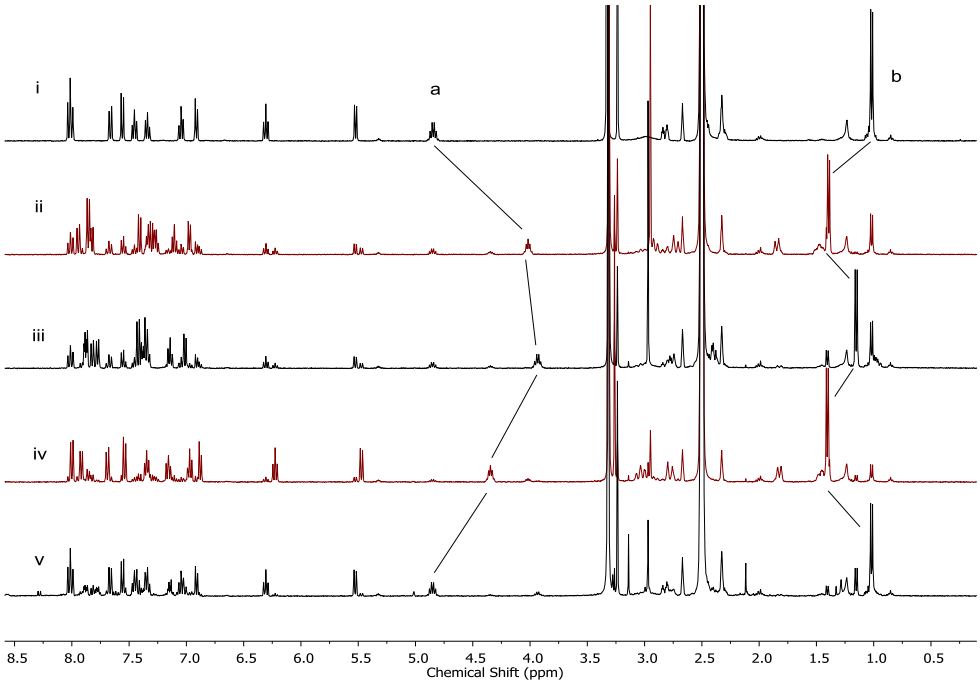

*Figure 3.3. ^{1}H-NMR spectra of a sample of **1** in DMSO-d_6 (c = 2.2 x 10^{-3} M). See Scheme 3.1 for the atom labeling. i) E-**1** before irradiation. ii) PSS 365 nm iii) 60 °C, 1h iv) PSS 365 nm. v) 100 °C, 120 min.*

When the NMR sample containing stable *Z*-**1** was once again irradiated at 365 nm, a new set of signals appeared indicative of unstable *E*-**1**, with a PSS_{365} ratio of 96:4. Upon heating to 100 °C, this unstable state was converted to the original isomer (stable *E*-**2**), and as a consequence, a 360° rotation was successfully achieved.

A similar rotational cycle was observed for motor **2** in THF-d_8. THF was chosen as low temperature studies were needed. Irradiation of a sample of **2** at 365 nm at -25 °C revealed the emergence of unstable *Z*-**2** (PSS_{365} = 77:23), which underwent THI to stable *Z*-**2** when the sample was allowed to warm to room temperature. Subsequent irradiation afforded unstable *E*-**2** (PSS_{365} > 99:1), which converted to the original isomer (stable *E*-**2**) when the sample was heated to 55 °C.

For motor **3**, for which the highest barriers for THI was calculated (*vide infra*), the first part of the cycle was found to be identical to that of motors **1** and **2**. Irradiation of an NMR sample of **3** in DMSO-d_6 at 365 nm at room temperature (PSS_{365} = 79:21) and subsequent heating to 100 °C showed the formation of stable *Z*-**3**. The sample was again irradiated to show the appearance of unstable *E*-**3** (PSS_{365} = 95:5), however, when it was heated, complete degradation was observed. Most likely, degradation is due to the high temperature required to trigger THI, owing to the high energy barrier for this compound.

Due to the low barrier for THI, unstable *Z*-**4** could only be observed when irradiated at -90 °C, which was performed in CD_2Cl_2. Even at this low temperature, unstable *Z*-**4** was observed to already undergo slow THI to form stable *Z*-**4**. At the same time, this isomer then undergoes a photochemical *E*-*Z* isomerization, forming unstable *E*-**4** over time. When warming the sample to -45 °C, stable *E*-**4** is again reformed, completing a 360° rotary cycle.

3.5 UV/vis and CD spectroscopy of 1-4

Next, the photochemical and thermal isomerization behavior of motors **1-4** were studied using UV/vis spectroscopy. All compounds show a broad absorption band with λ_{max} between 350 and 400 nm, which extends into the visible region (Figure 3.4). Very little solvatochromism (≤ 5 nm) was observed over a range of different solvents, including aromatic and protic solvents. The rotational cycle of motor **2** was additionally studied using CD spectroscopy. Its enantiomers were therefore separated using chiral supercritical fluid chromatography. The enantiomers could be identified by comparing their CD spectrum to the DFT calculated spectrum, generated using CAM-B3LYP/6-31+G(d,p) and a IEFPCM, DMSO solvation model (Figure 3.5). When a UV/vis sample of stable *E*-(*S*)-**1** in DMSO was irradiated at 365 nm, a bathochromic shift in both the UV and CD spectra could be observed, signifying the formation of unstable *Z*-(*S*)-**1**. Interestingly, isomerization could also be achieved with visible light of wavelengths up to 455 nm, albeit with a lower PSS, which is most likely due to the stronger absorption of the unstable isomer at longer wavelengths. Heating the sample to 60 °C leads to a blue shift of the band as unstable-*Z* is converted to stable-*Z*. The helicity is inverted in this step and as a consequence the sign of the CD absorption belonging to the π–π^* band is changed. Subsequent irradiation of this sample at 365 nm yields the unstable *E*-isomer, which is again accompanied by a characteristic bathochromic shift. The unstable *E*-isomer has the opposite CD sign as the starting stable *E*-isomer, which is expected as they have opposite helicity. Heating the sample to 100 °C completes the cycle, i.e. stable *E* is formed, which is accompanied by a hypsochromic shift.

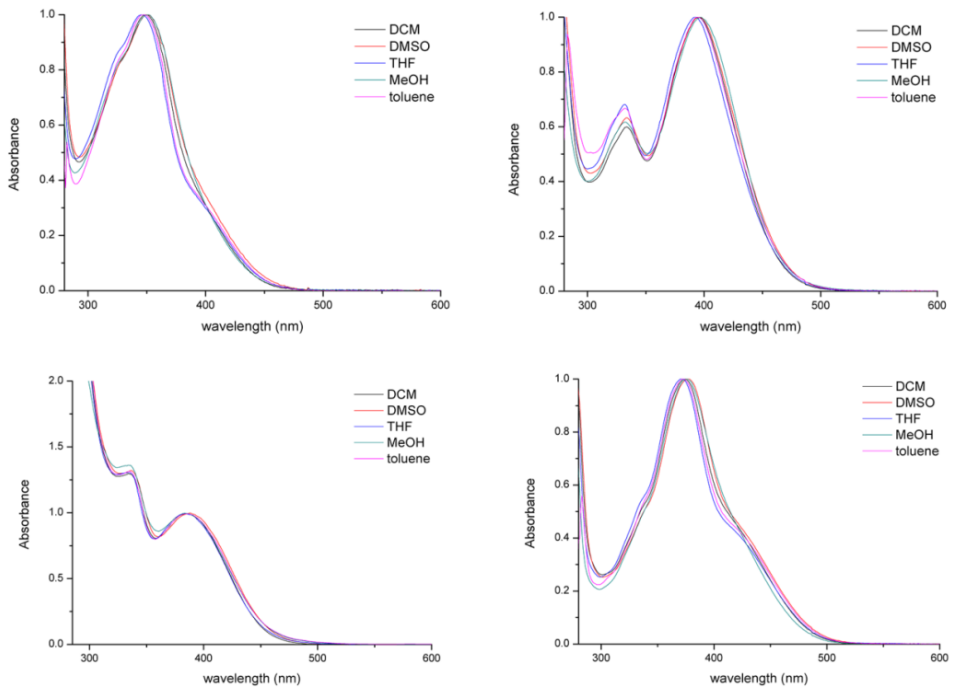

*Figure 3.4.Normalized UV/vis spectra of **1** (top left), **2** (top right), **3** (bottom left) and **4** (bottom right) in different solvents.*

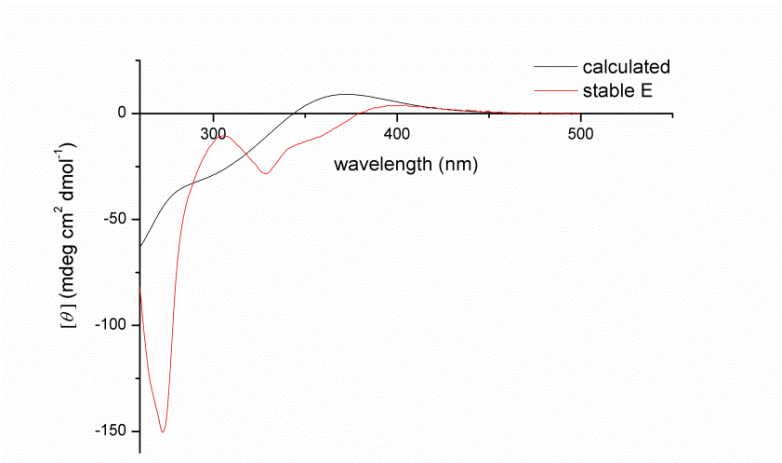

*Figure 3.5. Comparison of the DFT calculated spectrum of E-(S)-**1** with the experimentally obtained spectrum.*

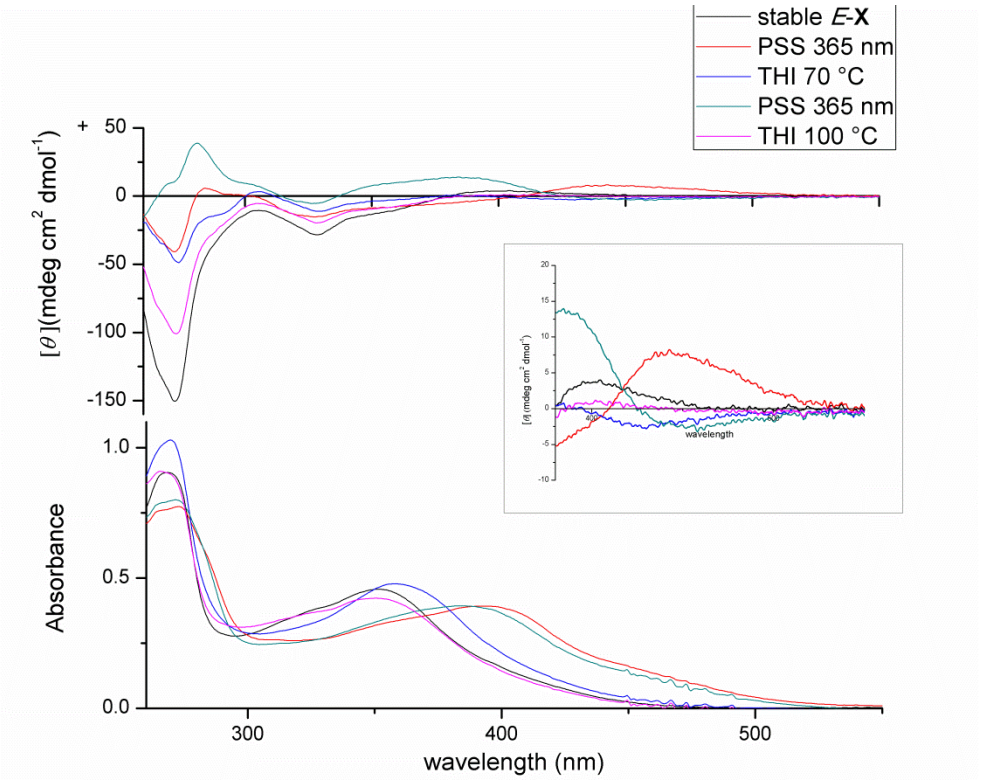

*Figure 3.6 CD and UV/vis spectra of the isomers in the rotation cycle of motor (S)-**1** in DMSO.*

UV/vis studies of motor **2** showed the same spectral changes as for motor **1**, with a bathochromic shift upon irradiation of the stable *E* isomer (Figure 3.7). In this case, isomerization was observed upon irradiation with wavelengths up to 505 nm, well into the visible region. Characterization of the isomerization behavior of motor **4** with UV/vis is more challenging due to its fast THI steps. Nonetheless, a bathochromic shift could be observed upon irradiation with wavelengths up to λ_{max}= 455 nm at -30 °C, most likely originating from the unstable *E* isomer (Figure 3.7). The unstable *Z* isomer undergoes THI which is too fast to follow at -30 °C (note that the calculated half-life at -30 °C is 38 ms).

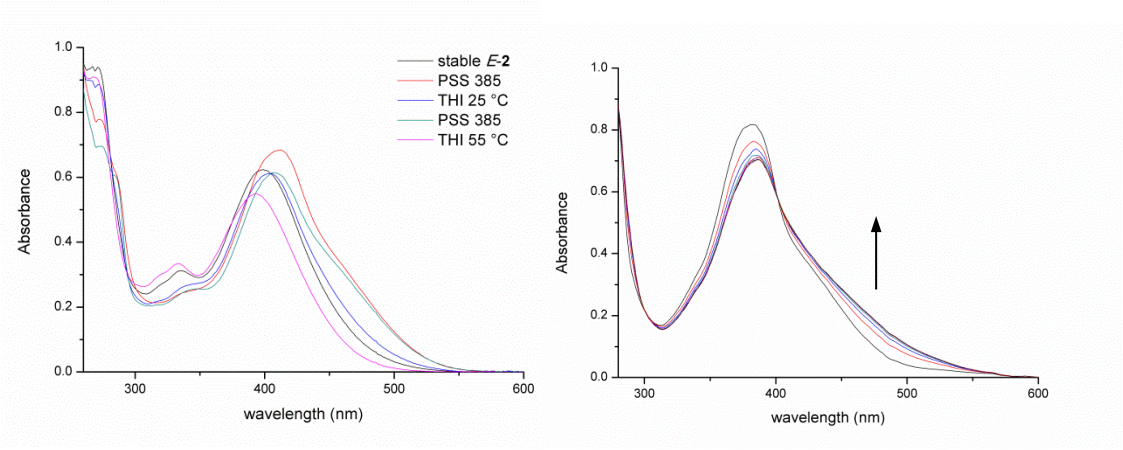

*Figure 3.7. UV/vis spectra of rotational cycle of motor **2** in THF (c = 3.5 x 10^{-5} M) (left), UV/vis spectra of stable E-**4** in CH_2Cl_2 (c = 4.7 × 10^{-5} M) at -30 °C upon irradiation with λ_{max}= 365 nm (right).*

Eyring analysis was performed to determine the activation parameters of the THIs of motors **1**, **2** and **4**. For compounds **1** and **2** the rate of THI was determined by following the change in absorbance at λ = 470 nm. For motor **4**, low temperature ^{1}H-NMR was used and only the barrier of from unstable *E*-**4** to stable *E*-**4** could be obtained as the THI of unstable *Z*-**4** is too fast to be measured. In each case, the rate of THI was determined at five temperatures, after which the activation parameters were obtained by using the Eyring equation (Table 3.2 and Figure 3.8). The Gibbs free energy barriers and half-lives of the respective unstable states are summarized in Table 3.2. All experimentally obtained barriers match those predicted by DFT, within a reasonable margin (≤ 3.4 kJ mol^{-1}). As predicted, the barriers for THI of the unstable *Z* isomers is lower for both motors **1** and **2**, and as a result the THI of unstable *E* is the rate limiting step in the rotational cycle. These results show that half-lives ranging from ms to days can be readily achieved by choosing the appropriate upper half.

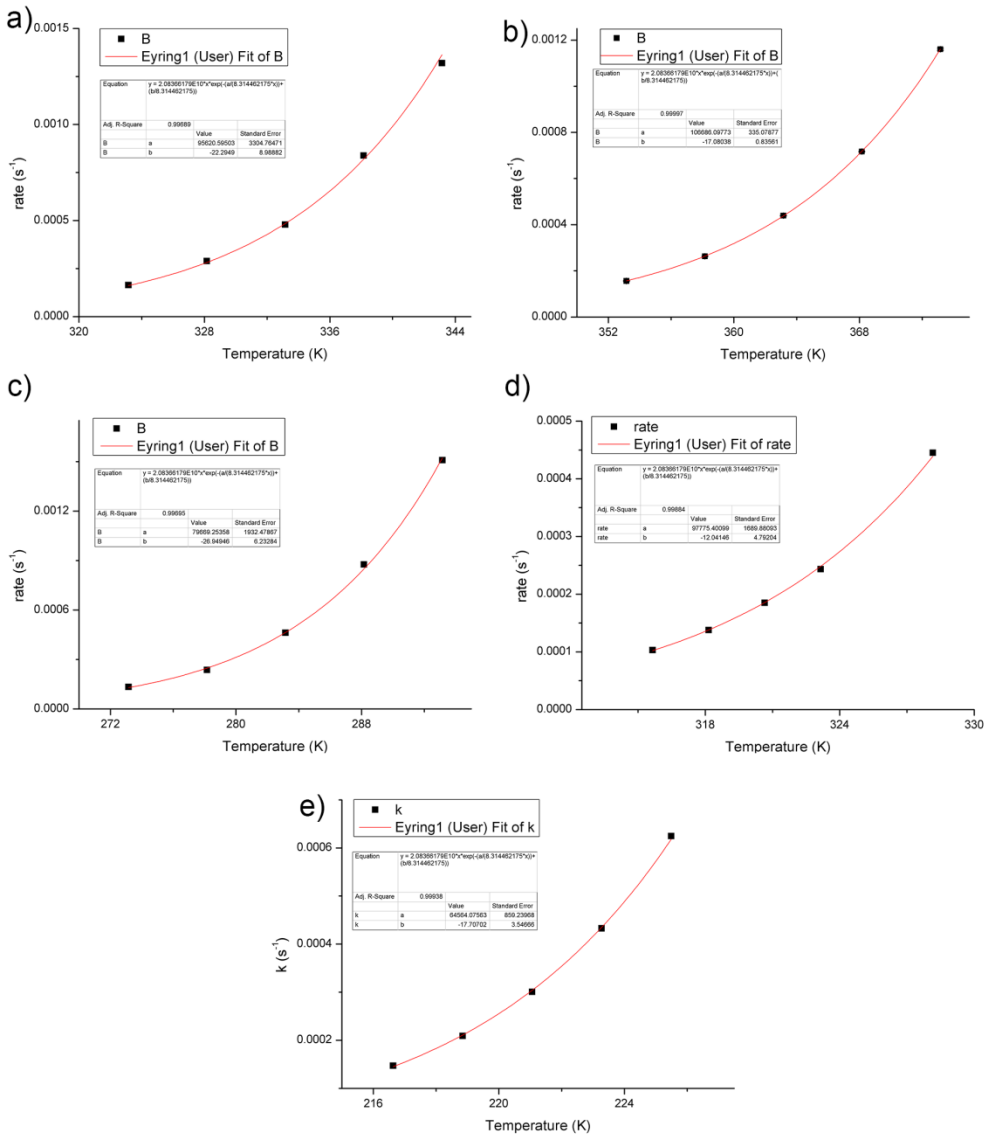

*Figure 3.8. Eyring plots of THI of a) Z-**1**, b) E-**1**, c) Z-**2**, d) E-**2**, e) E-**4**.*

	$\Delta^{\ddagger}H$ (Z) (kJ mol^{-1})	$\Delta^{\ddagger}S$ (Z) (J mol^{-1} K^{-1})	$\Delta^{\ddagger}G$ (Z) (kJ mol^{-1})	$t_{1/2}$	$\Delta^{\ddagger}H$ (E) (kJ mol^{-1})	$\Delta^{\ddagger}S$ (E) (J mol^{-1} K^{-1})	$\Delta^{\ddagger}G$ (E) (kJ mol^{-1})	$t_{1/2}$
1	95.6 ± 2.3	-22.3 ± 6.9	102.2 ± 0.3	50 ± 7h	106.7 ± 2.4	-17.1 ± 6.6	111.7 ± 0.5	105 ± 21d
2	79.7 ± 1.7	-26.9 ± 6.2	87.6 ± 0.1	455 ± 14s	97.8 ± 3.5	-12.0 ± 11.0	101.3 ± 0.3	35 ± 5h
4	-	-	-	-	64.6 ± 3.2	-17.7 ± 14.6	69.8 ± 1.1	305 ±148ms

*Table 3.2. Gibbs free energy barriers of THI and half-lives of the respective unstable states of motors **2-4**. All values of $\Delta^{\ddagger}G$ and $t_{1/2}$ are at 20 °C.*

Additionally, quantum yields of the photochemical isomerization steps ($\Phi_{s\rightarrow u}$) were estimated for motors **1** and **2** (Table 3.3). The rate of formation of the unstable states was determined by following the absorption increase at λ = 475 upon irradiation of a sample with a high enough concentration to absorb all incident light. To assess the efficiency of these motors with visible light, λ_{max}= 420 nm irradiation was used. The rates thus obtained were then compared to the rate of formation of Fe^{2+} from potassium ferrioxalate under identical condition to estimate the quantum yields (Table 3.3, see Experimental Procedures for details). The quantum yield for the reverse photochemical isomerization ($\Phi_{u\rightarrow s}$) could then be calculated using the PSS_{420} ratio and extinction coefficients at this wavelength. The obtained quantum yields are lower than those obtained with λ_{max}= 365 nm for second generation molecular motors based on overcrowded alkenes (5-20%).[38]

	Φ stable E → unstable Z	Φ unstable Z → stable E	Φ stable Z → unstable E	Φ unstable E - stable Z
1	2.3	0.67	2.1	0.32
2	1.2	0.35	3.0	0.18

Table 3.3. Quantum yields (%) of photochemical isomerization steps

3.6 Conclusions

In summary, a new, readily accessible, with easy to control rotary motion, molecular motor based on oxindole is presented which can be driven by visible light. A four-step rotation cycle was proposed based on DFT calculations and confirmed by a combination of

NMR, UV/vis and CD spectroscopy. Motors with four different upper halves were easily synthesized by a Knoevenagel condensation, allowing tuning of the half-life for THI and the overall motor speed from the millisecond regime to multiple days. Additionally, the oxindole scaffold provides an interesting handle for further functionalization, opening up new possibilities for application in biology and materials science.

3.7 Experimental procedures

For general remarks regarding experimental procedures see Chapter 2.

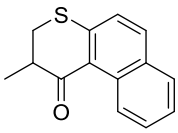

5

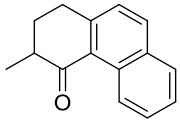

6

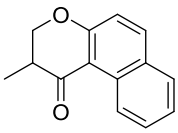

7

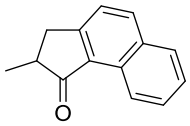

8

Ketones 5-7[35] and 8[37] were synthesized according to literature procedures.

General procedure for the synthesis of oxindole-based motors

The appropriate ketone (0.50 mmol) was dissolved in dry THF (2 ml) under N_2 atmosphere and the solution was cooled to 0 °C. $TiCl_4$ (0.75 mmol, 0.08 ml) was added dropwise and the resulting suspension was stirred for 5 min. *N*-methyloxindole (0.75 mmol, 110 mg) in THF (1 ml) was added and subsequently DBU (0.75 mmol, 0.11 ml) was added dropwise. The mixture was allowed to warm to room temperature and stirred for 2 h. The reaction was treated with 1M aq. HCl and extracted three times with EtOAc. The combined organic layers were washed with H_2O and brine, and dried over $MgSO_4$. The volatiles were removed *in vacuo* and the residue was purified by flash column chromatography (SiO_2, pentane/EtOAc 3-10%) to yield the corresponding motor.

(*E*)-1-methyl-3-(3-methyl-2,3-dihydrophenanthren-4(1H)-ylidene)indolin-2-one (*E*-1)

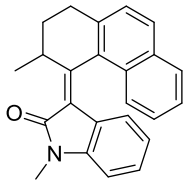

Motor *E*-**1** was isolated as a yellow solid (93 mg, 55%). ^{1}H NMR (400 MHz, DMSO-d_6) 8.00 (d, *J* = 8.5 Hz, 1H), 7.98 (d, *J* = 8.7 Hz, 1H) 7.65 (dd, *J* = 8.5, 1.2 Hz, 1H), 7.54 (s, 1H), 7.43 (d, *J* = 16.2 Hz, 1H), 7.32 (t, *J* = 7.7 Hz, 1H), 7.02 (t, *J* = 7.1 Hz, 1H), 6.89 (d, *J* = 7.7 Hz, 1H), 6.28 (t, *J* = 7.1 Hz, 1H), 5.51 (d, *J* = 7.7 Hz, 1H), 4.83 (dq, *J* = 13.7, 7.0 Hz, 1H), 3.22 (s, 3H), 2.85 – 2.75 (m, 1H), 2.46 – 2.40 (m, 1H), 2.36 – 2.23 (m, 1H), 1.07 – 0.94 (m, 1H), 1.00 (d, *J* = 6.8 Hz, 3H). ^{13}C NMR (101 MHz, DMSO-d_6) δ 166.6, 154.2, 142.2, 140.6, 131.6, 130.8, 129.7, 129.6, 128.7, 128.2, 127.2, 126.0, 125.2, 124.2, 122.4, 122.1, 121.2, 120.7, 107.9, 31.5,

28.9, 25.6, 20.7.HRMS (ESI+, *m/z*) Calcd for $C_{24}H_{22}NO$ $(M+H)^+$ = 340.16959, found 340.17004.

(*E*)-1-methyl-3-(2-methyl-2,3-dihydro-1H-benzo[f]chromen-1-ylidene)indolin-2-one (*E*-2)

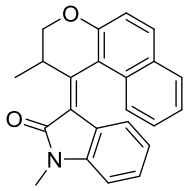

Motor *E*-**2** was isolated as an orange solid (79 mg, 63%). ^{1}H NMR (600 MHz, $CDCl_3$) δ 7.85 (d, *J* = 8.9 Hz, 1H), 7.80 (d, *J* = 7.9 Hz, 1H), 7.58 (d, *J* = 8.5 Hz, 1H), 7.31 (ddd, *J* = 8.1, 6.8, 1.2 Hz, 1H), 7.23 (ddd, *J* = 8.4, 6.8, 1.4 Hz, 1H), 7.11 (d, *J* = 8.9 Hz, 1H), 7.10 (td, *J* = 7.6, 1.2 Hz, 1H), 6.78 (d, *J* = 7.6 Hz, 1H), 6.47 (td, *J* = 7.7, 1.1 Hz, 1H), 6.06 (d, *J* = 7.6 Hz, 1H), 5.21 (qdd, *J* = 6.9, 3.7, 1.7 Hz, 1H), 4.46 (dd, *J* = 11.4, 3.7 Hz, 1H), 4.40 (dd, *J* = 11.4, 1.7 Hz, 1H), 3.33 (s, 3H), 1.26 (d, *J* = 6.9 Hz, 3H).^{13}C NMR (151 MHz, $CDCl_3$) δ 168.2, 155.1, 149.0, 142.3, 132.9, 130.2, 128.7, 128.6, 128.2, 127.3, 125.0, 124.5, 123.7, 122.3, 121.2, 118.2, 112.8, 107.3, 72.9, 29.3, 25.8, 16.2. HRMS (ESI+, *m/z*) Calcd for $C_{23}H_{20}NO_2$ $(M+H)^+$ = 342.14886, found 342.14920.

(*E*)-1-methyl-3-(2-methyl-2,3-dihydro-1H-benzo[f]thiochromen-1-ylidene)indolin-2-one (*E*-3)

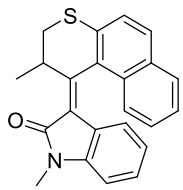

Motor *E*-**1** was isolated as an orange solid (122 mg, 68 %). ^{1}H NMR (400 MHz, $CDCl_3$) δ 7.84 (d, *J* = 8.5 Hz, 1H), 7.81 (d, *J* = 8.9 Hz, 1H), 7.72 (d, *J* = 8.5 Hz, 1H), 7.47 (d, *J* = 8.6 Hz, 1H), 7.39 (ddd, *J* = 8.1, 6.8, 1.2 Hz, 1H), 7.30 – 7.25 (m, 1H), 7.03 (td, *J* = 7.7, 1.2 Hz, 1H), 6.71 (d, *J* = 7.8 Hz, 1H), 6.34 (td, *J* = 7.7, 1.1 Hz, 1H), 5.65 (p, *J* = 6.7 Hz, 1H), 5.60 (d, *J* = 7.8 Hz, 1H), 3.33 (dd, *J* = 12.1, 6.8 Hz, 1H), 3.30 (s, 3H), 2.74 (dd, *J* = 12.0, 6.0 Hz, 1H), 1.16 (d, *J* = 6.7 Hz, 3H). ^{13}C NMR (101 MHz, $CDCl_3$) δ 167.9, 153.2, 142.6, 137.3, 131.6, 131.3, 130.4, 129.3, 128.7, 128.6, 127.7, 126.9, 125.5, 124.3, 124.0, 123.4, 121.9, 121.6, 107.5, 36.0, 33.4, 26.0, 18.2. HRMS (ESI+, *m/z*) Calcd for $C_{23}H_{20}NOS$ $(M+H)^+$ = 358.12601, found 358.12648.

(*E*)-1-methyl-3-(2-methyl-2,3-dihydro-1H-cyclopenta[a]naphthalen-1-ylidene)indolin-2-one (*E*-4)

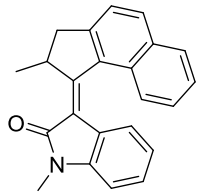

Motor *E*-**1** was isolated as an orange solid (36 mg, 22%). ^{1}H NMR (400 MHz, $CDCl_3$) δ 7.99 (d, *J* = 8.0 Hz, 1H), 7.97 (d, *J* = 7.9 Hz, 1H), 7.63 (d, *J* = 8.4 Hz, 1H), 7.59 (d, *J* = 8.2 Hz, 1H), 7.52 (t, *J* = 7.5 Hz, 1H), 7.42 (t, *J* = 7.6 Hz, 1H), 7.17 (t, *J* = 7.7 Hz, 1H), 6.85 (d, *J* = 7.8 Hz, 1H), 6.66 (t, *J* = 7.7 Hz, 1H), 6.39 (d, *J* = 7.7 Hz, 1H), 4.66 (p, *J* = 6.6 Hz, 1H), 3.50 (dd, *J* = 15.7, 5.9 Hz, 1H), 3.37 (s, 3H), 2.77 (d, *J* = 15.7 Hz, 1H), 1.30 (d, *J* = 6.8 Hz, 3H). ^{13}C NMR (101 MHz, $CDCl_3$) δ 171.4, 164.6, 153.2, 145.3, 137.5, 135.5, 135.3, 131.8, 131.5, 130.3, 130.1, 129.5, 128.3, 127.7, 126.7, 124.8, 123.2, 122.4, 109.8, 46.3, 44.2, 28.5, 22.1. HRMS (ESI+, *m/z*) Calcd for $C_{23}H_{20}NO$ $(M+H)^+$ = 326.15394, found 326.15443.

(*Z*)-1-methyl-3-(3-methyl-2,3-dihydrophenanthren-4(1H)-ylidene)indolin-2-one (*Z*-1)

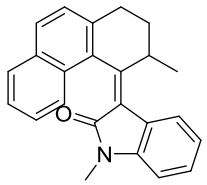

Motor *E*-**1** (10 mg, 0.029 mmol) was dissolved in 20 ml CH_2Cl_2 and irradiated with λ_{max} = 365 nm for 3 h at 5 °C. CH_2Cl_2 was removed *in vacuo* and the residue was dissolved in EtOAc. The mixture was heated at reflux for 2 h in the dark. The volatiles were removed *in vacuo* and the residue was purified by flash column chromatography (SiO_2, pentane/EtOAc 3-10%) to yield motor *Z*-**1** (5 mg, 50%) as an yellow solid. ^{1}H NMR (600 MHz, $CDCl_3$) δ 7.97 (d, *J* = 8.2 Hz, 1H), 7.84 (d, *J* = 7.4 Hz, 1H), 7.82 (d, *J* = 8.2 Hz, 1H), 7.77 (d, *J* = 7.6 Hz, 1H), 7.41 (t, *J* = 8.1 Hz, 1H), 7.38 – 7.31 (m, 3H), 7.13 (td, *J* = 7.7, 1.1 Hz, 1H), 6.85 (d, *J* = 7.7 Hz, 1H), 3.97 (h, *J* = 7.2 Hz, 1H), 2.73 (ddd, *J* = 14.3, 4.2, 2.9 Hz, 1H), 2.55 (td, *J* = 13.7, 4.7 Hz, 1H), 2.38 (dddd, *J* = 12.7, 7.7, 4.7, 2.8 Hz, 1H), 1.29 (d, *J* = 7.0 Hz, 3H), 1.13 (tdd, *J* = 13.0, 7.4, 4.2 Hz, 1H). ^{13}C NMR (151 MHz, $CDCl_3$) δ 165.6, 153.5, 143.7, 139.3, 132.9, 131.9, 131.7, 129.3, 128.4, 128.3, 126.3, 125.4, 124.9, 124.5, 123.9, 123.4, 122.7, 121.6, 107.8, 35.2, 29.8, 29.7, 25.8, 20.4. HRMS (ESI+, *m/z*) Calcd for $C_{24}H_{22}NO$ $(M+H)^+$ = 340.16959, found 340.16997.

(*Z*)-1-methyl-3-(2-methyl-2,3-dihydro-1H-benzo[f]chromen-1-ylidene)indolin-2-one (*Z*-2)

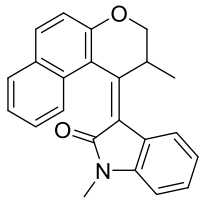

Motor *E*-**2** (10 mg, 0.029 mmol) was dissolved in CH_2Cl_2 (20 ml) and the mixture was degassed by purging with N_2 for 20 min. After cooling to -50 °C, the mixture was irradiated with λ_{max} = 365 nm overnight. It was allowed to warm to room temperature and stirred for 1h. The volatiles were removed *in vacuo* and the residue was purified by flash column chromatography (SiO_2, pentane/EtOAc 3-10%) to yield motor *Z*-**2** (5 mg, 50%) as an orange solid. ^{1}H NMR (600 MHz, $CDCl_3$) δ 7.92 (d, *J* = 7.6 Hz, 1H), 7.79 (d, *J* = 8.9 Hz, 1H), 7.75 (d, *J* = 7.4 Hz, 1H), 7.64 (d, *J* = 7.6 Hz, 1H), 7.37 – 7.28 (m, 3H), 7.10 (t, *J* = 8.2 Hz, 1H), 7.04 (d, *J* = 8.9 Hz, 1H), 6.88 (d, *J* = 7.8 Hz, 1H), 4.45 (dd, *J* = 11.4, 3.8 Hz, 1H), 4.33 (dd, *J* = 11.6, 1.9 Hz, 1H), 3.97 – 3.89 (m, 1H), 3.17 (s, 3H), 1.40 (s, 3H). ^{13}C NMR (151 MHz, $CDCl_3$) δ 165.3, 153.9, 147.0, 143.3, 133.2, 132.9, 128.7, 128.3, 128.3, 126.6, 124.5, 123.7, 123.1, 123.0, 122.2, 121.5, 117.7, 113.0, 108.1, 71.4, 32.4, 26.0, 15.9. HRMS (ESI+, *m/z*) Calcd for $C_{23}H_{20}NO_2$ $(M+H)^+$ = 342.14886, found 342.14934.

Quantum yield determination

The photon flux of a Thorlabs model M420F2 LED was determined by measuring the production of ferrous ions from potassium ferrioxalate as described in Chapter 2 (5.31 x 10^{-5} mmol photons per second).

A sample of motor **1** or **2** was irradiated with λ_{max} = 420 nm light under identical conditions as with the actinometry at a concentration high enough to absorb all incident light (Abs_{420} > 2). In the case of *E*-**2**, the sample was irradiated at -15 °C to prevent the THI to occur. The formation of unstable states was monitored over time by following the absorbance increase at λ = 475 nm. The molar absorptivity of the unstable states at λ = 475 nm was used to calculate the concentration increase. The initial concentration increase was plotted versus time (Figure 3.9) and the slope, the rate of formation of the unstable state, was obtained by linear fitting to the equation y = ax + b using Origin software. The photochemical quantum yield ($\Phi_{s\rightarrow u}$) was then calculated using the photon flux of this specific light source previously determined at identical conditions in the actinometry. The quantum yield of the reverse reaction ($\Phi_{u\rightarrow s}$) at λ = 420 nm can then be calculated using equation 1, in which [stable]/[unstable] is the ratio of both states at PSS_{420} (Table 3.4).

$$\frac{[\text{stable}]}{[\text{unstable}]} = \frac{\Phi_{(u\rightarrow s)}\varepsilon_u}{\Phi_{(s\rightarrow u)}\varepsilon_s} \qquad (1)$$

	PSS_{420} (unstable/stable)	ε_{420} (stable) (M^{-1} cm^{-1})	ε_{420} (unstable) (M^{-1} cm^{-1})
E-**1**	51:49	2.53×10^3	8.73×10^3
Z-**1**	67:33	5.61×10^3	1.77×10^4
E-**2**	62:38	8.25×10^3	1.72×10^4
Z-**2**	94:6	1.60×10^4	1.66×10^4

*Table 3.4. PSS ratios and molar absorptivities of motors **1** and **2** at 420 nm.*

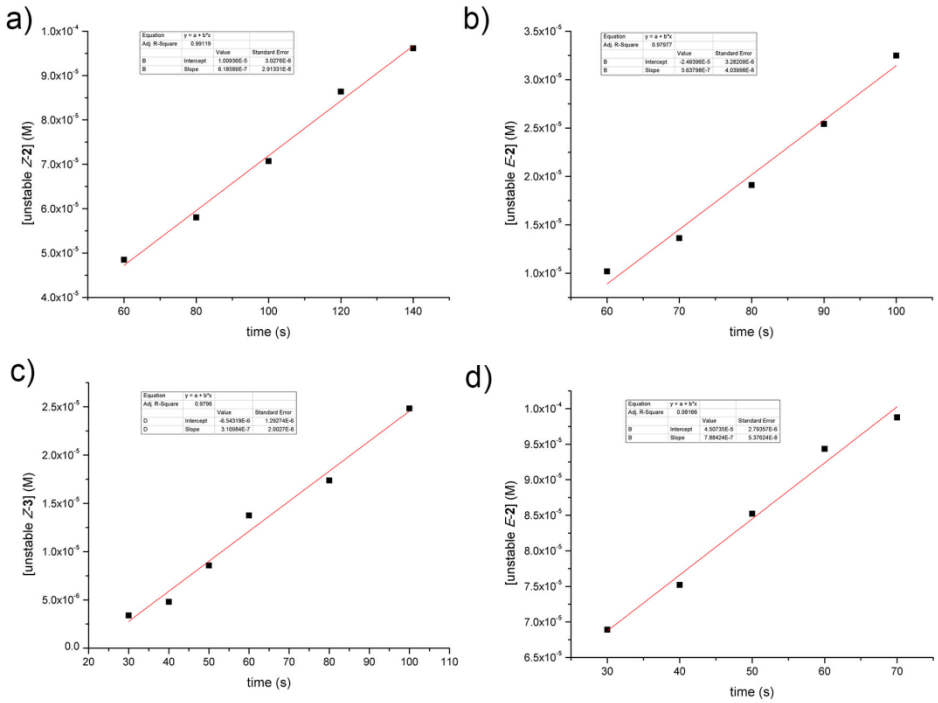

*Figure 3.9 Linear fit of photochemical formation of unstable states by irradiation with λ = 420 nm. a) stable E-**1** (c = 1.6 x 10^{-4} M in DMSO) b) stable Z-**1** (c = 5.7 x 10^{-4} M in DMSO) c) stable E-**2** (c = 1.6 x 10^{-4} M in THF) d) stable Z-**2** (c = 3.4 x 10^{-4} M in THF).*

3.8 References

[1] V. Balzani, A. Credi, F. M. Raymo, J. F. Stoddart, *Angew. Chem. Int. Ed.* **2000**, *39*, 3348–

3391.

[2] K. Kinbara, T. Aida, *Chem. Rev.* **2005**, *105*, 1377–1400.

[3] W. R. Browne, B. L. Feringa, *Nat. Nanotechnol.* **2006**, *1*, 25–35.

[4] E. R. Kay, D. A. Leigh, *Angew. Chem. Int. Ed.* **2015**, *54*, 10080–10088.

[5] V. Balzani, A. Credi, M. Venturi, *Molecular Devices and Machines: Concepts and Perspectives for the Nanoworld: Second Edition*, Wiley-VCH, Weinheim, **2008**.

[6] J. P. Sauvage, P. Gaspard, Eds. , *From Non-Covalent Assemblies to Molecular Machines*, Wiley-VCH, Weinheim, **2010**.

[7] C. J. Bruns, J. F. Stoddart, *The Nature of the Mechanical Bond: From Molecules to Machines*, John Wiley & Sons, Inc., Hoboken, NJ, **2016**.

[8] S. Kassem, T. van Leeuwen, A. S. Lubbe, M. R. Wilson, B. L. Feringa, D. A. Leigh, *Chem. Soc. Rev.* **2017**, *46*, 2592–2621.

[9] D. Roke, S. J. Wezenberg, B. L. Feringa, *Proc. Natl. Acad. Sci. U. S. A.* **2018**, 201712784.

[10] T. van Leeuwen, A. S. Lubbe, P. Štacko, S. J. Wezenberg, B. L. Feringa, *Nat. Rev. Chem.* **2017**, *1*, 0096.

[11] J. Chen, F. K.-C. Leung, M. C. A. Stuart, T. Kajitani, T. Fukushima, E. van der Giessen, B. L. Feringa, *Nat. Chem.* **2017**, *10*, 132–138.

[12] Q. Li, G. Fuks, E. Moulin, M. Maaloum, M. Rawiso, I. Kulic, J. T. Foy, N. Giuseppone, *Nat. Nanotechnol.* **2015**, *10*, 161–165.

[13] J. T. Foy, Q. Li, A. Goujon, J.-R. Colard-Itté, G. Fuks, E. Moulin, O. Schiffmann, D. Dattler, D. P. Funeriu, N. Giuseppone, *Nat. Nanotechnol.* **2017**, *12*, 540–545.

[14] R. Eelkema, M. M. Pollard, J. Vicario, N. Katsonis, B. S. Ramon, C. W. M. Bastiaansen, D. J. Broer, B. L. Feringa, *Nature* **2006**, *440*, 163–163.

[15] J. Wang, B. L. Feringa, *Science* **2011**, *331*, 1429–1432.

[16] K.-Y. Chen, O. Ivashenko, G. T. Carroll, J. Robertus, J. C. M. Kistemaker, G. London, W. R. Browne, P. Rudolf, B. L. Feringa, *J. Am. Chem. Soc.* **2014**, *136*, 3219–3224.

[17] B. L. Feringa, N. Koumura, R. W. J. Zijlstra, R. A. van Delden, N. Harada, *Nature* **1999**, *401*, 152–155.

[18] N. Koumura, E. M. Geertsema, M. B. Van Gelder, A. Meetsma, B. L. Feringa, *J. Am. Chem. Soc.* **2002**, *124*, 5037–5051.

[19] J. C. M. Kistemaker, P. Štacko, J. Visser, B. L. Feringa, *Nat. Chem.* **2015**, *7*, 890–896.

[20] M. M. Pollard, A. Meetsma, B. L. Feringa, *Org. Biomol. Chem.* **2008**, *6*, 507–512.

[21] M. Klok, N. Boyle, M. T. Pryce, A. Meetsma, W. R. Browne, B. L. Feringa, *J. Am. Chem. Soc.* **2008**, *130*, 10484–10485.

[22] S. J. Wezenberg, K. Y. Chen, B. L. Feringa, *Angew. Chem. Int. Ed.* **2015**, *54*, 11457–11461.

[23] A. Faulkner, T. van Leeuwen, B. L. Feringa, S. J. Wezenberg, *J. Am. Chem. Soc.* **2016**, *138*, 13597–13603.

[24] T. van Leeuwen, W. Danowski, S. F. Pizzolato, P. Štacko, S. J. Wezenberg, B. L. Feringa, *Chem. - Eur. J.* **2018**, *24*, 81–84.

[25] D. Bléger, S. Hecht, *Angew. Chem. Int. Ed.* **2015**, *54*, 11338–11349.

[26] A. Cnossen, L. Hou, M. M. Pollard, P. V. Wesenhagen, W. R. Browne, B. L. Feringa, *J. Am. Chem. Soc.* **2012**, *134*, 17613–17619.

[27] T. van Leeuwen, J. Pol, D. Roke, S. J. Wezenberg, B. L. Feringa, *Org. Lett.* **2017**, *19*, 1402–1405.

[28] R. A. van Delden, N. Koumura, A. Schoevaars, A. Meetsma, B. L. Feringa, *Org. Biomol. Chem.* **2003**, *1*, 33–35.

[29] L. Greb, J.-M. Lehn, *J. Am. Chem. Soc.* **2014**, *136*, 13114–13117.

[30] L. Greb, A. Eichhöfer, J. M. Lehn, *Angew. Chem. Int. Ed.* **2015**, *54*, 14345–14348.

[31] M. Guentner, M. Schildhauer, S. Thumser, P. Mayer, D. Stephenson, P. J. Mayer, H. Dube, *Nat. Commun.* **2015**, 8406.

[32] L. A. Huber, K. Hoffmann, S. Thumser, N. Böcher, P. Mayer, H. Dube, *Angew. Chem. Int. Ed.* **2017**, *56*, 14536–14539.

[33] S. Luňák, P. Horáková, A. Lyčka, *Dye. Pigment.* **2010**, *85*, 171–176.

[34] A. Cnossen, J. C. M. Kistemaker, T. Kojima, B. L. Feringa, *J. Org. Chem.* **2014**, *79*, 927–935.

[35] J. C. M. Kistemaker, S. F. Pizzolato, T. van Leeuwen, T. C. Pijper, B. L. Feringa, *Chem. - Eur. J.* **2016**, *22*, 13478–13487.

[36] J. Vicario, A. Meetsma, B. L. Feringa, *Chem. Commun.* **2005**, 5910–5912.

[37] U. Dietrich, M. Hackmann, B. Rieger, M. Klinga, M. Leskelä, *J. Am. Chem. Soc.* **1999**, *121*, 4348–4355.

[38] J. Conyard, A. Cnossen, W. R. Browne, B. L. Feringa, S. R. Meech, *J. Am. Chem. Soc.* **2014**, *136*, 9692–9700.